Finite-Amplitude Lagrangian-Mean Wave Activity Diagnostics Applied to the Baroclinic Eddy Life Cycle

ABRAHAM SOLOMON

Center for Ocean–Land–Atmosphere Studies, Calverton, Maryland

GANG CHEN

Cornell University, Ithaca, New York

JIAN LU

Center for Ocean–Land–Atmosphere Studies, Calverton, Maryland

(Manuscript received 1 November 2011, in final form 15 May 2012)

ABSTRACT

Lagrangian-mean wave activity diagnostics are applied to the nonlinear baroclinic eddy life cycle in a simple general circulation model of the atmosphere. The growth of these instabilities through baroclinic conversion of potential temperature gradients and their subsequent barotropic decay can exhibit two distinct life cycles. One life cycle results in equatorward propagation of the growing eddy, anticyclonic wave breaking, and a poleward shift of the mean jet. The second life cycle is distinguished by limited equatorward propagation and cyclonic wave breaking on the poleward flank of the jet. Using a conservative finite-amplitude, Lagrangian-mean wave activity (negative pseudomomentum) to quantify wave growth and propagation reveals more details about the life cycles than could be discerned from eddy kinetic energy (EKE) or other Eulerian metrics. It is shown that the distribution of pseudomomentum relative to the latitude of the axis of the jet can be used to provide a clear distinction between the two life cycles at an early stage in their development and, hence, a prediction for the subsequent shift of the jet. This suggests that the distribution of pseudomomentum may provide some predictability for the atmospheric annular modes.

1. Introduction

The breaking of atmospheric waves has long been recognized as an important and complex process, crucial to the advancement in our understanding of the short-term weather forecast, seasonal and intraseasonal predictability, and the general circulation of the atmosphere (McIntyre and Palmer 1983). Simply stated, atmospheric wave breaking is the irreversible deformation of material surfaces. In the upper troposphere, waves radiated by occluding tropospheric depressions can break as they propagate upward and equatorward, redistributing angular momentum and heat. Many papers have been written about this phenomenon, employing a wide variety of diagnostics, modeling efforts, and insightful observations. Recent advances in the Lagrangian theory of wave–mean flow interaction (Nakamura and Solomon 2010) provide a new perspective on this classic problem. Using diagnostics based on the distribution of material surfaces, wave breaking can be more readily quantified.

When a baroclinic jet becomes unstable, its subsequent evolution may follow two very distinct paths, first noted by Simmons and Hoskins (1980) and subsequently dubbed life cycle 1 (LC1) and life cycle 2 (LC2) in Thorncroft et al. (1993). The dichotomy between the life cycles has profound consequences for the evolution of the zonal mean wind. One of the most remarkable things about this instability is that identical perturbations, growing on two nearly indistinguishable, zonally symmetric background states, may evolve along these very distinct paths (Thorncroft et al. 1993). Hartmann and Zuercher (1998) demonstrated that a slight change in background shear could induce an abrupt transition from LC1 to LC2.

Corresponding author address: Abraham Solomon, Center for Ocean–Land–Atmosphere Studies, 4041 Powder Mill Road, Suite 302, Calverton, MD 20705-3106.
E-mail: solomon@cola.iges.org

DOI: 10.1175/JAS-D-11-0294.1

This investigation will examine the results of a set of experiments, which explore a parameter space spanning this transition, using the combined diagnostic tools of a Lagrangian-mean, finite-amplitude wave activity and the Eliassen–Palm (EP) flux. Previous studies have either used EP flux and linear wave theory (Hartmann and Zuercher 1998; Limpasuvan and Hartmann 2000) or finite amplitude diagnostics whose flux cannot be directly related to the tendency of the mean flow (Magnusdottir and Haynes 1996; Esler and Haynes 1999). Because this new Lagrangian framework is compatible with the familiar transformed Eulerian mean, it provides a simple way to augment a conventional analysis of wave–mean flow interaction.

The life cycles have been characterized in various different ways. Simmons and Hoskins (1980) recognized that LC2 exhibits much slower decay of eddy kinetic energy (EKE) than LC1. This difference in persistence was also noted by Thorncroft et al. (1993) when looking at wave activity. There is also a pronounced difference in the direction of wave propagation between the life cycles. Hartmann and Zuercher (1998) showed that the enhanced equatorward propagation exhibited in LC1 can be attributed to differences in the refractive indices associated with the zonal mean background state. Magnusdottir and Haynes (1996) employed a finite-amplitude wave activity and noted that the meridional excursion exhibited during LC1 was partly nonlinear advection and not completely a wave propagation phenomenon. These differences in the propagation of waves and the dissipation of wave activity result in a poleward shift of the jet in LC1 relative to LC2, as noted by many authors. This jet shift is associated with a meridional dipole in angular momentum, which has a barotropic structure and projects onto the atmospheric annular mode (Limpasuvan and Hartmann 2000). This paper will complement these observations with a demonstration that such a dipole is exhibited in the distribution of angular pseudomomentum as well, a result which is not evident from the distribution of EKE.

The annular modes represent the primary pattern of atmospheric variability in the extratropics, whose phase has major influences on regional climate. There is no consensus on the fundamental underlying cause for the variability of these pressure and wind patterns; however, improved predictability would be invaluable for medium-range weather forecasting and projections of climate change. Several authors have drawn a connection between wave breaking and variability of the annular modes. Esler and Haynes (1999) constructed a wave-breaking index based on the meridional flux of wave activity and used it to relate variability of the waves to the state of the jet. Riviere and Orlanski (2007) relate life cycles and wave breaking to the structure of the storm track and the North Atlantic Oscillation, a pattern closely related to the annular mode. Another recent study by Strong and Magnusdottir (2008) also developed an index of wave breaking and showed that it provided some skill for predicting the phase of the annular mode. In this paper, a new index based on the distribution of wave activity is introduced. This index is shown to clearly distinguish the two life cycles across a suite of experiments, without the need to calculate any fluxes of momentum.

The next section reviews the diagnostics used to evaluate the experiments in this study. The third section describes the simplified atmospheric model employed to carry out the simulations. The fourth section will detail one pair of experiments that exemplify this transition. The fifth section explores the parameter space spanned by zonal wavenumber and barotropic shear in order to determine any systematic variations in the life cycle and develop a method for objectively distinguishing them. A discussion of the predictability of jet shifts using Lagrangian-mean diagnostics and comparison with more conventional Eulerian alternatives follows.

2. Diagnostics

This study will employ the finite-amplitude Lagrangian-mean wave activity (negative pseudomomentum) introduced in Nakamura and Solomon (2010), which employs the potential vorticity equivalent latitude $\phi_{\rm eq}$ as a meridional coordinate (Butchart and Remsberg 1986). The wave activity at time t is defined as

$$A(\phi_{\rm eq}, z, t) = \frac{1}{2\pi a \cos\phi_{\rm eq}}\left(\int_{Q(\phi_{\rm eq})\le q(\phi')} q\, dS' - \int_{\phi_{\rm eq}\le\phi'} q\, dS'\right), \tag{1}$$

where q is the potential vorticity, the area element $dS' = a^2 \cos\phi' d\lambda d\phi'$, $a = 6378$ km the radius of the earth, and $Q(\phi_{\rm eq})$ is the Lagrangian-mean potential vorticity. The equivalent latitude is defined such that the areas covered by the two integrals are equal. That is to say,

$$\int_{Q(\phi_{\rm eq})\le q(\phi')} dS' = \int_{\phi_{\rm eq}\le\phi'} dS', \tag{2}$$

which specifies the value of Q as a function of $\phi_{\rm eq}$. The quasigeostrophic (QG) potential vorticity (PV) is

$$q = f + \mathbf{k}\cdot(\nabla\times\mathbf{v}) + \frac{f}{\rho_0}\frac{\partial}{\partial z}\left[\frac{\rho_0(\theta-\theta_0)}{\partial\theta_0/\partial z}\right], \tag{3}$$

where f is the Coriolis parameter, $\mathbf{k}$ the unit upward pointing normal vector, $\mathbf{v}$ the geostrophic wind, $\theta(\lambda, \phi, z, t)$ is potential temperature, $\theta_0(z, t)$ the layer mean potential temperature, and $\rho_0 \propto \exp(-z/H)$.

Consider the conservation of PV, using the nondivergent geostrophic wind $\mathbf{v}$:

$$\frac{\partial q}{\partial t} = -\mathbf{v}\cdot\nabla q = -\nabla\cdot(\mathbf{v}q). \tag{4}$$

If q is conserved, the first term in the definition of A [Eq. (1)] is constant following the motion of a parcel of air, and the tendency of wave activity is due only to the flux of PV across the fixed, bounding equivalent latitude:

$$\frac{\partial}{\partial t}(A\cos\phi) = -\frac{1}{2\pi a}\int_{\phi\le\phi'}\frac{\partial q}{\partial t}\,dS = -\cos\phi\overline{\tilde{v}\tilde{q}}. \tag{5}$$

Here overbars denote zonal means and tildes denote deviations from zonal means. Assuming that the waves are geostrophic and ignoring the divergence associated with the gradient in f, it can be shown that

$$\cos\phi\overline{\tilde{v}\tilde{q}} = \frac{1}{\rho_0}\nabla\cdot\mathbf{F}, \tag{6}$$

where $\mathbf{F}$ is the QG EP flux

$$\mathbf{F} = (F^{\phi}, F^{z}) = \rho_0\cos\phi[-\overline{\tilde{u}\tilde{v}}, f\overline{\tilde{v}\tilde{\theta}}/(\partial\bar{\theta}/\partial z)] \tag{7}$$

and $\nabla\cdot\mathbf{F} = (a\cos\phi)^{-1}\,\partial(\cos\phi F^{\phi})/\partial\phi + \partial F^{z}/\partial z$. Thus Eq. (5) is approximately

$$\frac{\partial}{\partial t}(A\cos\phi) = -\frac{1}{\rho_0}\nabla\cdot\mathbf{F}, \tag{8}$$

as demonstrated in Nakamura and Solomon (2010). Furthermore, the QG transformed Eulerian-mean zonal momentum equation on the sphere as derived in Pfeffer (1987) is

$$\frac{\partial}{\partial t}(\bar{u}\cos\phi) = \frac{1}{\rho_0}\nabla\cdot\mathbf{F} + f\bar{v}_R\cos\phi \tag{9}$$

so that the Coriolis torque associated with the residual circulation $\bar{v}_R(\phi, z, t)$ balances the tendencies of wave activity and the zonal mean wind:

$$\frac{\partial}{\partial t}(\bar{u} + A) = f\bar{v}_R. \tag{10}$$

In practice the three terms in Eq. (10) tend to be of comparable magnitude, the nature of the balance being determined by the aspect ratio of the wave forcing (Pfeffer 1987). For tall, narrow forcing, in the absence of irreversible processes, the right-hand side tends to be negligible; hence Eq. (10) is referred to as a non-acceleration theorem (Nakamura and Zhu 2010a).

3. Model

The model used in this set of experiments is an atmosphere-only model, which employs the Geophysical Fluid Dynamics Laboratory spectral dynamical core on 30 vertical sigma levels specified as

$$\sigma_k \equiv p(k)/p_s = \exp[\gamma(30-k)/30], \quad \text{for} \quad k = 0, \ldots, 30, \tag{11}$$

where $p(k)$ is pressure on the kth level, p_s the surface pressure, and $\gamma = \log(2\times10^{-2})$. There is no external heating or dissipation during the baroclinic eddy life cycle, except for hyperdiffusion to damp the smallest scales. The initial condition is expressed in terms of pseudoheight, which is a linear function of log pressure, $z = -H\log(p/p_0)$, where the scale height $H = 7.5$ km and reference pressure $p_0 = 1000$ hPa. The initial zonal wind is specified to resemble the experiments in Hartmann and Zuercher (1998):

$$u(\lambda, \phi, z) = u_0(\phi, z) + u_s(\phi) + u_m(\lambda, \phi, z), \tag{12}$$

where u_0 is a baroclinic jet, u_s a barotropic jet, and u_m the velocity anomaly associated with the normal mode of zonal wavenumber m scaled to a standard amplitude for each case. The specified profile for the baroclinic jet is

$$u_0(\phi, z) = U_0\sin^3(\pi\sin^2\phi)\left[z/z_T\exp\left(-\frac{z^2/z_T^2-1}{2}\right)\right], \quad \phi>0. \tag{13}$$

Here the parameters are $U_0 = 45$ m s^{-1} and $z_T = 13$ km. The barotropic component of the initial wind field is

$$u_s(\phi) = U_s\left\{\exp\left[-\left(\frac{\phi-\phi_e}{\Delta\phi}\right)^2\right] - \exp\left[-\left(\frac{\phi-\phi_p}{\Delta\phi}\right)^2\right]\right\}, \tag{14}$$

where $\phi_e = 20°$, $\phi_p = 50°$, and $\Delta\phi = 12.5°$. The barotropic shear parameter U_s is systematically varied among the experiments in order to explore its effect on the evolution of the normal mode perturbation. The temperature and surface pressure are derived from geostrophic and hydrostatic balance such that the temperature is in thermal wind balance with the initial zonal wind, following the method described in Polvani and Esler (2007). The lower boundary of the model is specified as a geopotential

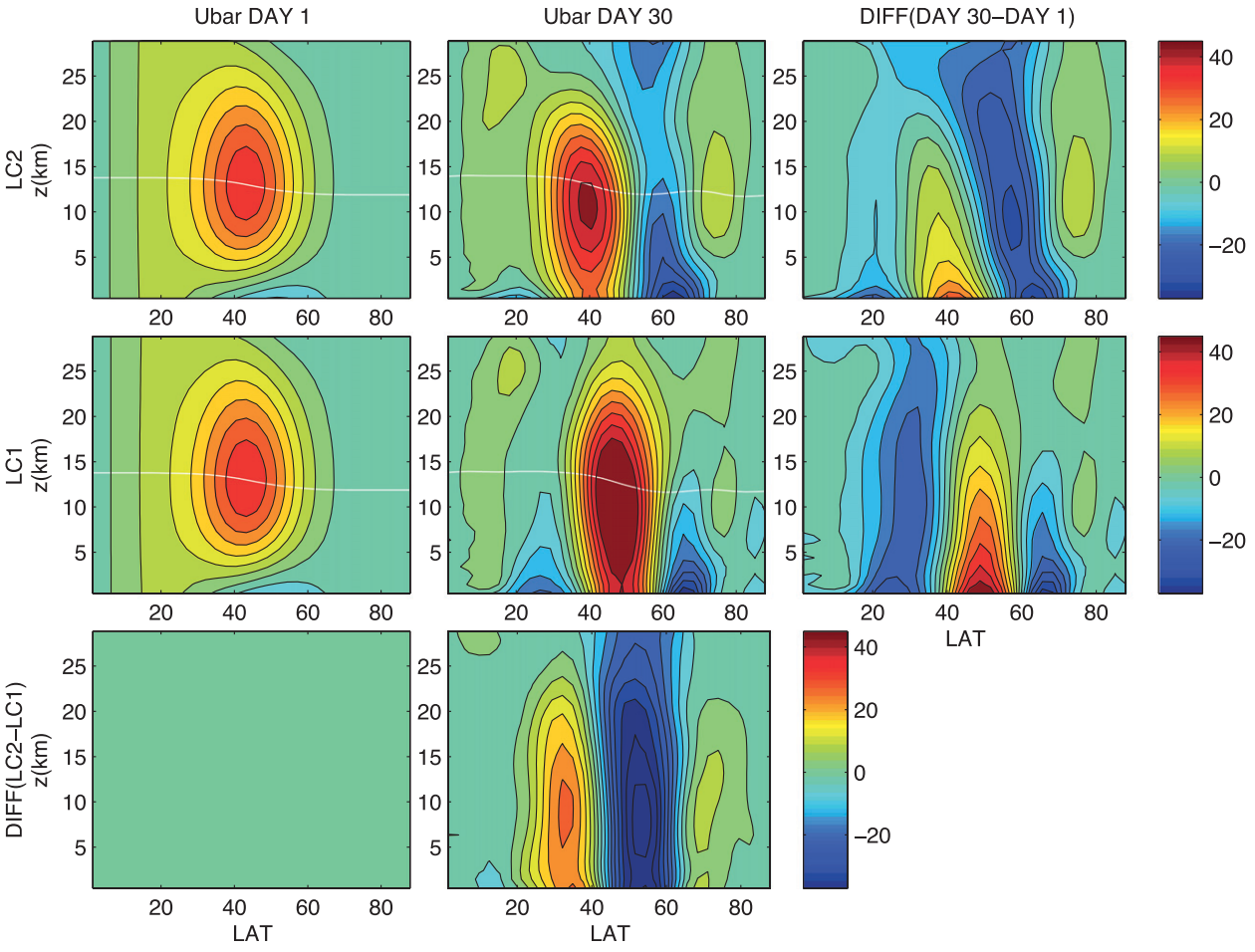

FIG. 1. Zonal mean wind $\overline{u}$ (m s^{-1}) plotted in the Northern Hemisphere (NH) meridional plane for the (middle) LC1 and (top) LC2 cases, and (bottom) their difference at (left) the initial state (day 1) for each experiment, (middle) the final state (day 30), and (right) the net evolution of each case respectively.

surface $\Phi(\phi, p_s) = 0$, which allows the surface pressure to vary in time. Geopotential height is calculated as

$$\Phi(\phi, p) = \int_p^{p_0} \frac{RT_r(p')}{p'}\, dp' - \int_0^{\phi} (af + u \tan\phi')u\, d\phi', \tag{15}$$

where the reference temperature at the equator is

$$T_r(p) = T_s + \frac{\Gamma_0}{(z_T^{-\alpha} + z^{-\alpha})^{1/\alpha}} \tag{16}$$

for $T_s = 300$ K, $\Gamma_0 = -6.5$ K km^{-1}, and $\alpha = 10$.

4. One transition case

In this section one pair of experiments that clearly depict the transition from LC1 to LC2 will be examined in detail. The initial states for these two experiments are very similar. Both have a small zonal wavenumber-6 perturbation to the zonally symmetric background flow. The only difference between the two is the value chosen for the barotropic shear parameter U_s. The LC1 case, which has slightly lower shear $U_s = 9.5$ m s^{-1}, is associated with anticyclonic wave breaking. Anticyclonic wave breaking refers to the northeast–southwest tilting of troughs on the equatorward flank of the jet, as illustrated with maps of Θ on PV surfaces in Thorncroft et al. (1993, Fig. 7). Whereas, the LC2 case, in which $U_s = 10$ m s^{-1}, exhibits so-called cyclonic wave breaking. Cyclonic breaking involves the cutting off of nearly circular vortices on the poleward side of the jet, which become homogenized in their interiors and tend to be long-lived (Thorncroft et al. 1993, Fig. 9). As we see in Fig. 1, the two cases have nearly identical initial zonal mean wind distributions (left column), differing from each other by less than 1 m s^{-1} within the domain (bottom left). However, this subtle difference in initial conditions

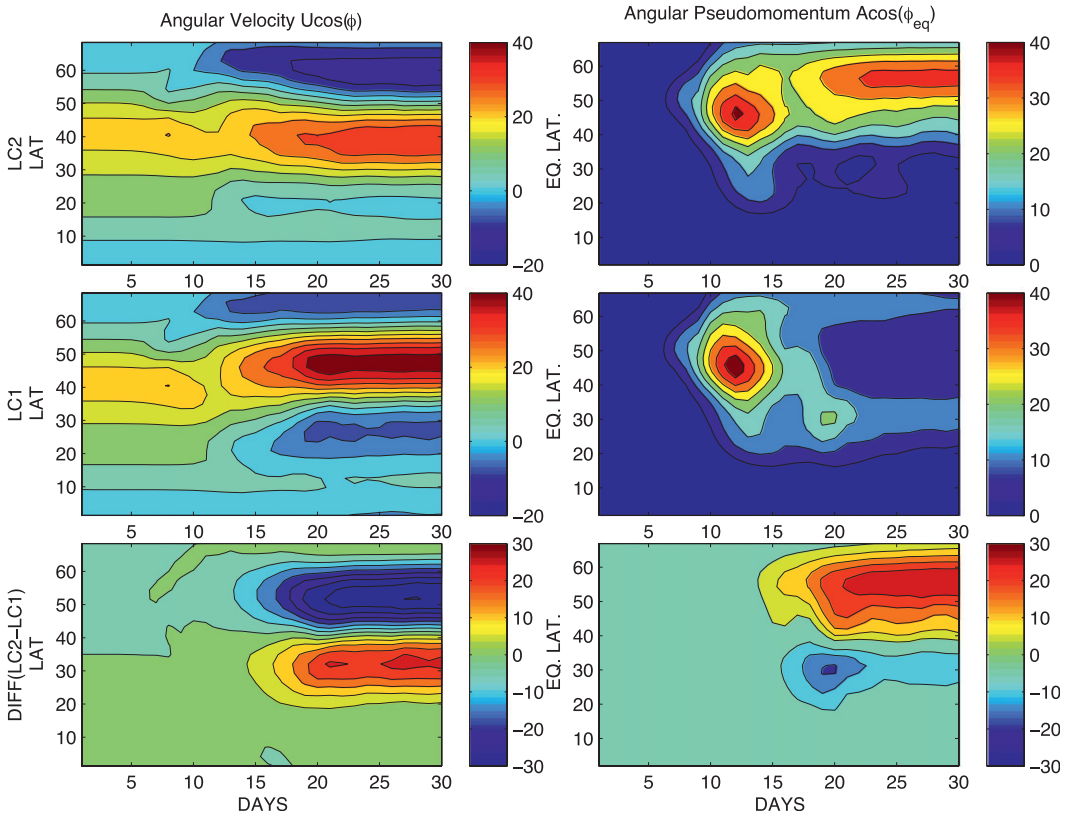

FIG. 2. (left) Barotropic angular velocity $[\overline{u}]\cos\phi$ (m s^{-1}) and (right) barotropic angular pseudomomentum $[A]\cos\phi_{\rm eq}$ (m s^{-1}) plotted for (top) LC2, (middle) LC1, and (bottom) their difference. Note that the differences are plotted with distinct color bars.

results in very different zonal mean wind fields on day 30 (middle panel), at the end of the simulation. The evolution of the high shear case (LC2) is best described as a sharpening of the jet with a slight equatorward shift (top right). The low shear case (LC1) results in a significant poleward shift of the jet; the jet also narrows in latitudinal extent and intensifies (middle right). The difference between the two final states may be characterized as a dipole with a node at 55°, whose structure is fairly uniform below 15 km (bottom middle). These are basic features of the life cycles, which have been discussed in previous papers and here will be explained in the context of wave activity.

In the past decade a number of studies have investigated the vacillation of the extratropical eddy-driven jet as an equivalent barotropic process. Limpasuvan and Hartmann (2000) showed that the annular modes, the principal mode of variability in the extratropical circulation, exhibit largely barotropic structure in both the height field and zonal winds. This variability is manifest as a meridional dipole structure associated with tropospheric wave breaking, with centers of action located between 30°–40°N and 50°–60°N. Subsequent work by Lorenz and Hartmann (2001) and Vallis et al. (2004) underscored the equivalent barotropic nature of the annular modes and the potential for understanding their variability with stochastic models driven by eddy forcing.

To illustrate this perspective and draw a connection between these life cycle experiments and the detailed analysis of observations and models undertaken by previous investigators, we consider the barotropic angular velocity in Fig. 2 (left panels). The barotropic angular velocity is simply a pressure weighted vertical average of the zonal wind:

$$[\overline{u}](\phi,t)\cos\phi = \frac{1}{p_s}\int_0^{p_s}\overline{u}(p,\phi,t)\cos\phi\, dp. \qquad (17)$$

Results from the LC2 experiment (top) show the slight equatorward shift of the mean westerlies, with the development of zonal mean easterlies on the poleward flank. LC1 (middle) shows a pronounced poleward shift after day 12 and progressive strengthening and sharpening of the jet between days 15 and 20. The difference between the mean winds in these two life cycles (bottom) exhibits a dipole structure reminiscent of the

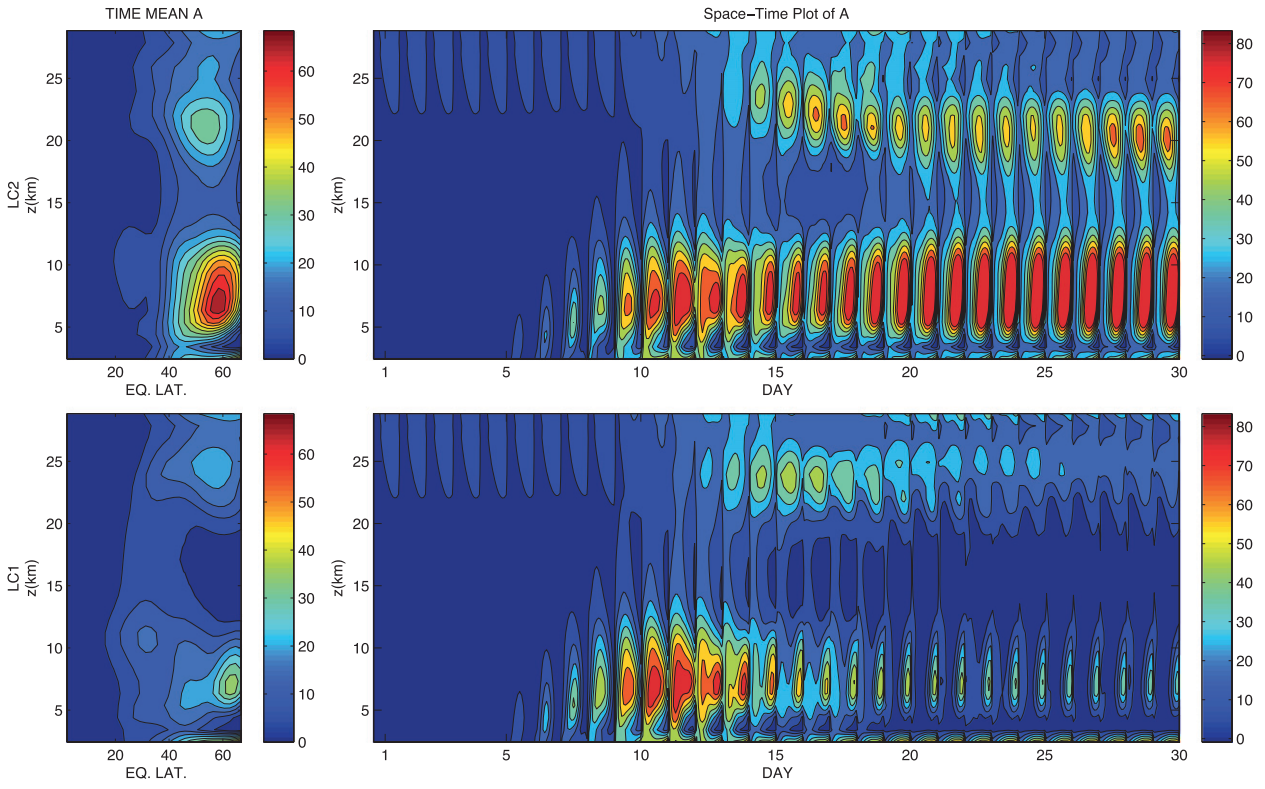

FIG. 3. (left) The time mean wave activity is plotted in the NH meridional plane for the (bottom) LC1 and (top) LC2 cases. (right) All 30 snapshots of A are concatenated to illustrate its temporal evolution.

difference between extreme states of observed annular modes.

Recent investigations into the annular modes have emphasized the role of wave breaking. It now appears clear that the high phase of the annular mode is associated with anticyclonic breaking of synoptic-scale waves (Benedict et al. 2004; Riviere and Orlanski 2007; Strong and Magnusdottir 2008). Employing the Lagrangian-mean wave activity to visualize the role of waves in these experiments provides a new perspective on the evolution of the circulation in this wave-breaking process. The barotropic wave activity $[A](\phi_{eq}, t)\cos\phi_{eq}$ is plotted in the right panels of Fig. 2. LC2 (top) and LC1 (middle) have similar distributions of angular pseudomomentum prior to day 15 with a localized maximum centered around 50°N. LC1 shows enhanced equatorward propagation between days 15 and 20, then steady decay of $[A]$ at all latitudes as the simulation progresses. In contrast, LC2 exhibits a brief period of transience in wave activity around day 15, followed by a poleward shift of the maximum in $[A]$ and steady increase until day 20. This new quasi-equilibrium state of wave activity persists for the duration of the experiment. These differences are comparable to the distinction between LC1 and LC2 made by Simmons and Hoskins (1980), which emphasized that both cases attain similar maximum levels of eddy kinetic energy, but in the LC2 case the EKE dissipates much more slowly. However, the meridional propagation of the eddies is not as clear from EKE, which exhibits only a single maximum that tends to follow the latitude of maximum winds (not shown). Using this Lagrangian-mean finite-amplitude wave activity, the meridional dipole in angular pseudomomentum mirroring that of velocity (bottom right) can be discerned in the difference between the two life cycles. These opposing dipoles illustrate the exchange of pseudomomentum for angular momentum underlying this wave–mean flow interaction in a way that cannot be reproduced from linearized Eulerian metrics that do not possess an exact nonacceleration theorem (Solomon and Nakamura 2012).

We have seen that the distinction between the two cases is clearly depicted by the temporal evolution of wave activity. In Fig. 3 the time average distribution of wave activity is shown on the left. The two cases have similar distributions of mean wave activity: however, it is apparent that the LC2 case has larger time-averaged wave activity and the LC1 case has broader meridional extent. In the panels on the right, the temporal evolution of wave activity for the two cases is illustrated by concatenating 30 snapshots of wave activity in the meridional plane. This

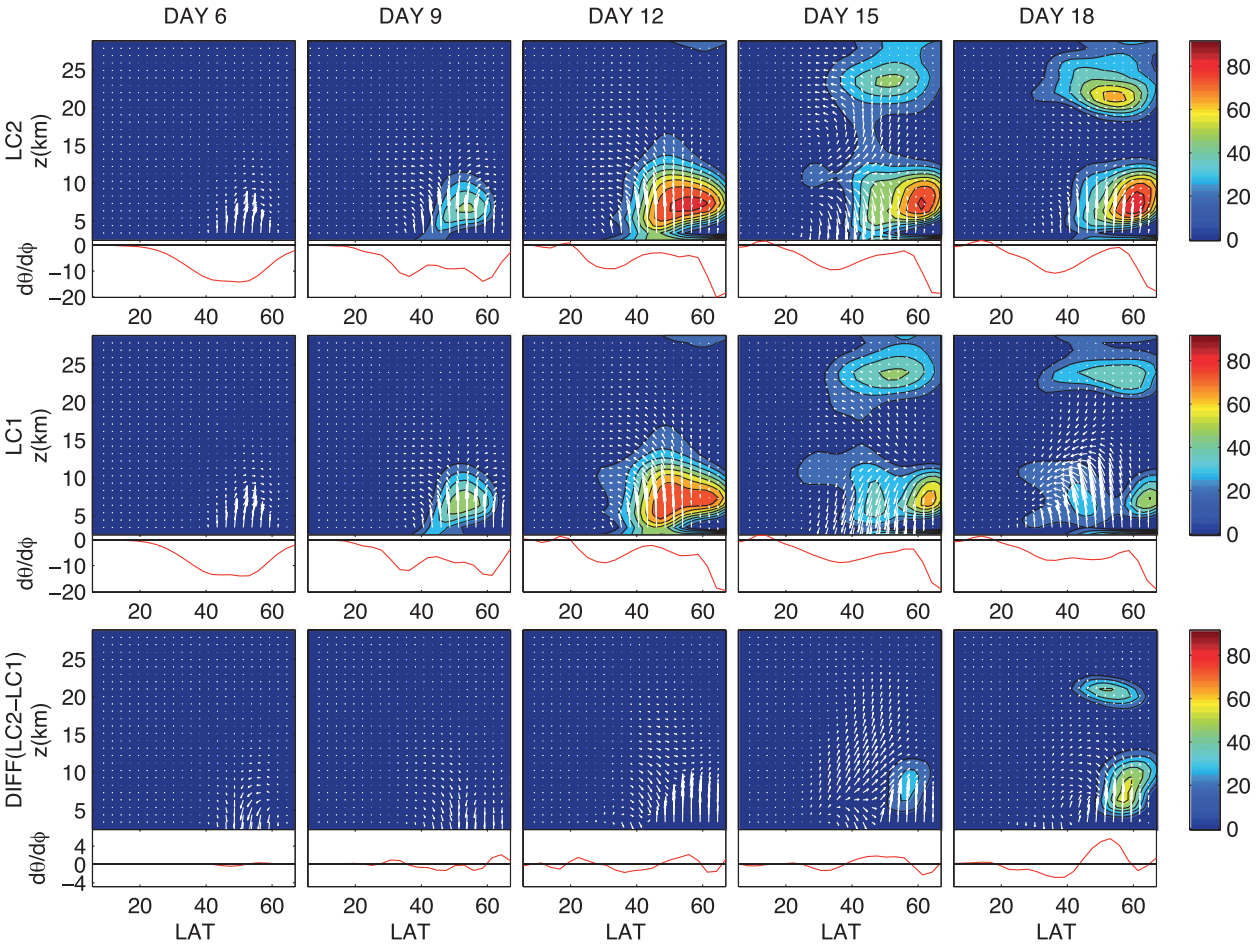

FIG. 4. Five snapshots of wave activity (m s^{-1}), in the meridional plane, for (top) the LC2 case and (middle) the LC1 case on days 6, 9, 12, 15, and 18 of the simulation. The EP-flux vectors are overlain in white and the zonal mean potential temperature gradient [K (°lat)$^{-1}$] on the 723-mb surface is plotted in red below each panel. (bottom) The difference between the two cases (LC2 − LC1) for each day.

space–time diagram illustrates that the growth of wave activity between days 6 and 12 is very comparable between the two cases, attaining nearly identical maximum values in the upper troposphere. However, the subsequent evolution follows extremely different paths. In the LC1 case (bottom right) the waves begin to decay around day 12 and continue to diminish at all vertical levels as the simulation proceeds. In contrast, the LC2 case (top right) shows some transience in the midtroposphere around day 12, but then the tropospheric waves grow again until they have equilibrated around day 24. Additionally, the secondary maximum of wave activity in the stratosphere, which emerges in both simulations around day 12, grows and descends in LC2 while it has all but vanished by day 20 in LC1. This figure indicates that the crucial difference in the evolution of these simulations must manifest itself between days 10 and 15, so in this interval we will examine the dynamics more closely, using the combined diagnostic power of A and the EP flux.

Figure 4 shows five snapshots of wave activity between days 6 and 18 of each experiment. In the top row A is plotted in the meridional plane for the LC2 case with the EP-flux vectors overlain. Plotted beneath each snapshot is the near surface potential temperature gradient, which represents the wave source. On day 6 the waves are still negligibly small, but a region of eddy heat flux between 40° and 60°N coincides with the latitudes of maximum magnitude temperature gradient. By day 9 a measurable density of pseudomomentum has accumulated between 5 and 10 km, which continues to expand on day 12. The temperature gradient has developed a bimodal structure although upward flux persists throughout the extratropics with divergence aloft. On day 15 the maximum in wave activity has shifted toward the pole and the EP flux is now poleward everywhere except on the

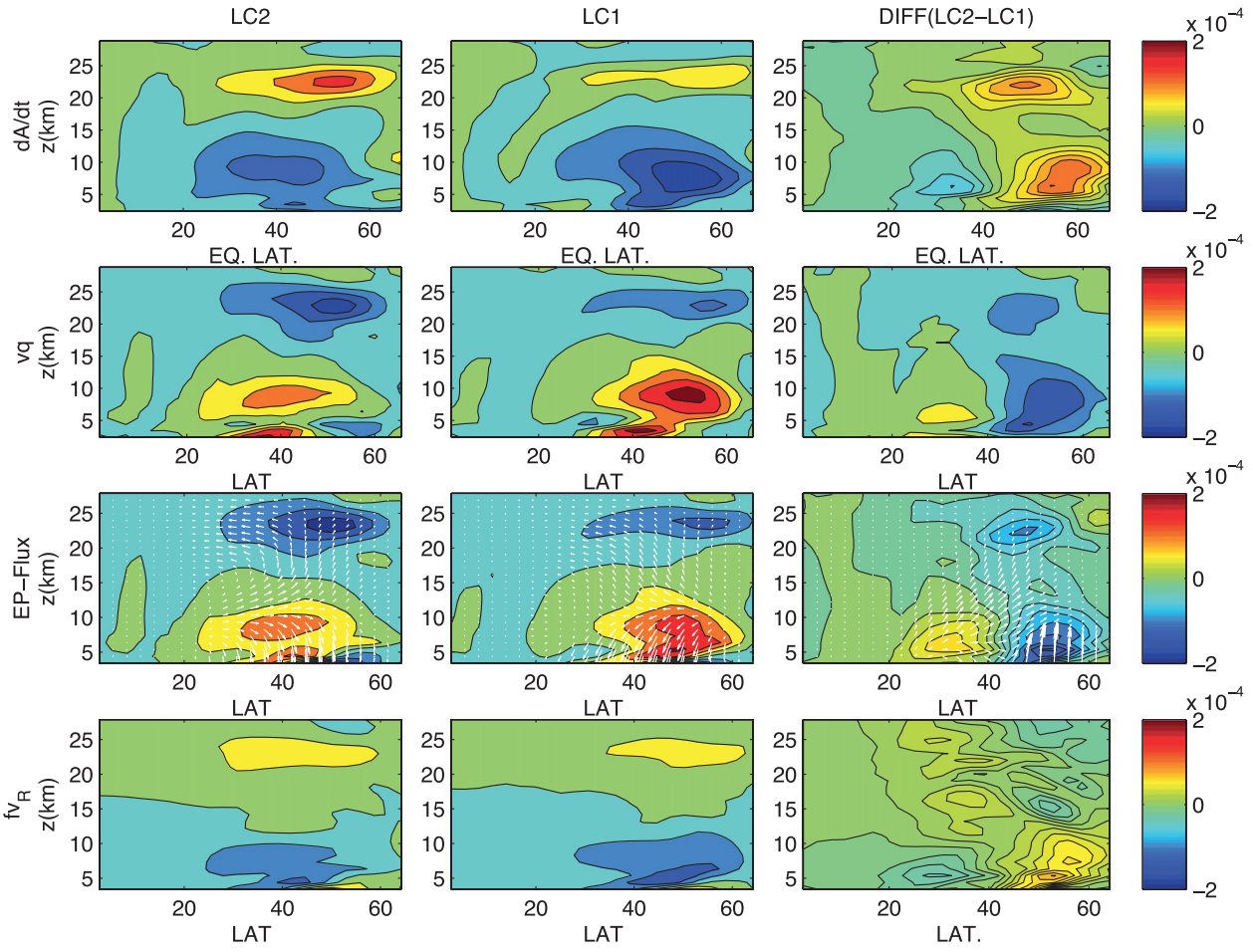

FIG. 5. (first row) The tendency of wave activity on day 15 (m s^{-1}) (same color bar and units for each row) is plotted in the meridional plane for the (left) LC2 and (middle) LC1 cases and (right) their difference (LC2 − LC1). (second row) As in first row, but for the zonal mean poleward flux of eddy PV. (third row) EP-flux convergence in colors with the flux vectors overlain in white. (fourth row) Coriolis torque due to the residual circulation.

equatorward flank of the secondary maximum in wave activity developing between 20 and 25 km. Day 18 depicts very strong wave activity north of 40°N in both the troposphere and stratosphere. The orientation of this locus for wave activity, directly above a region of enhanced meridional temperature gradient and upward EP flux, contributes to the persistence of waves in the LC2 case.

Corresponding snapshots for the LC1 case are plotted in the middle panels and the difference between the two cases is displayed in the lower panels. Until day 12 there is little difference visible between the two cases in either wave activity or surface temperature gradients. On day 12, although the distributions of wave activity are still nearly identical, there is a greater heat flux at high latitudes in the LC2 case. By day 15 a perceptible difference in the density of pseudomomentum in the troposphere near 60°N has emerged. Furthermore, the EP flux on day 15 in the LC1 case is everywhere equatorward, opposite to that of the LC2 case. On day 18 the wave activity in the LC1 case has diminished dramatically: strong equatorward fluxes below 15 km continue to erode the remaining wave activity at high latitudes. At this point the difference in wave activity density between the two cases has also become visible in the stratosphere and a sizable discrepancy in surface temperature gradients has emerged.

On day 15 the two life cycles exhibit substantial differences in the distribution and tendency of momentum, which can be estimated by a variety of methods that we compare here. In the top row of Fig. 5 the tendency of wave activity is estimated by taking the difference between its density on days 16 and 14. Values from the LC2 experiment (left top) show a dipole structure in the vertical with waves decaying below 15 km and growing above, consistent with the vertical propagation of waves at this stage of the life cycle

discussed by Thorncroft et al. (1993). The tendency of wave activity in the LC1 case (middle top) displays a structure largely similar to the high shear case; however, the magnitudes are very different. To illustrate more clearly the discrepancy in their structure, the difference between their tendencies is plotted on the right. We find an increasing deficit of wave activity in the LC1 case, relative to the LC2 case, throughout the high latitudes of the free atmosphere. The second row of Fig. 5 shows the instantaneous zonal mean poleward flux of PV, which in theory should be the negative of the wave activity tendency. The agreement in the spatial structure of these two quantities reassures us that our understanding of the quantity A is valid. In addition to these basic confirmations, we can also see a meridional dipole structure in the difference between these instantaneous tendencies on day 15.

In the third row of Fig. 5 we see the EP-flux divergence, which agrees well with the PV flux. Overlain are the EP-flux vectors, which help to interpret their divergence. In the LC2 case, poleward flux at 35°N diverges strongly both upward and downward, suggesting reflection of waves near 10 km. In the LC1 case, the pattern is reversed with equatorward flux at 60°N, diverging in the vertical again around 10 km. It is worth noting here that these three measures of the tendency of momentum rely on very different assumptions and approximations, yet they exhibit reasonable quantitative agreement. In particular, the fact that the quasigeostrophic EP-flux convergence matches the tendency of A underscores the point that this Lagrangian framework is consistent with the familiar flux-based, Eulerian, linearized diagnosis. The lower panels show the Coriolis torque associated with the residual circulation. Note that this term is the same order of magnitude as the other tendency terms and typically opposes them. Both cases indicate poleward circulation at upper levels and an equatorward branch near the surface. The difference between the two shows a stronger circulation near the surface north of 40°N in the LC1 case, which contributes to the difference in surface potential temperature gradients.

Previous investigations have employed linear wave theory and refractive indices to distinguish the evolution of the two life cycles (e.g., Hartmann and Zuercher 1998). Planetary waves tend to propagate toward regions of high refractive index n^2 and can be reflected where the index vanishes (Karoly and Hoskins 1982):

$$n^2(\phi, z, t) = \frac{\partial \overline{q}(\phi, z)/\partial \phi}{a(\overline{u} - c_p)} + N^2 m^2, \tag{18}$$

where the Brunt–Väisälä frequency $N^2 = (g/\theta_0)\, \partial\theta_0/\partial z$ and c_p is the phase velocity of the wave. The dominant term in the refractive index is proportional to the meridional gradient of zonal-mean PV, so in regions where the PV gradient vanishes or becomes negative, wave propagation is suppressed according to linear theory. Great insights into wave–mean flow interaction have been developed within the framework of refraction and critical layer theory (e.g., Killworth and McIntyre 1985): however, linear theory cannot address all aspects of the baroclinic life cycle once wave breaking and mixing begin to significantly modify the mean state (Hartmann and Zuercher 1998). To investigate the changing PV gradients in the evolution of the life cycles we will consider both the zonal-mean and Lagrangian-mean PV in Fig. 6. By differentiating Eq. (1) twice with respect to latitude (enforcing $\phi_{\rm eq} = \phi$), it can be shown that the two mean PV gradients differ owing to a contribution from the wave activity:

$$\frac{\partial \overline{q}}{\partial \mu} = \frac{\partial Q}{\partial \mu} + \frac{\partial^2 A \cos\phi}{\partial \mu^2}, \tag{19}$$

where $\mu = \sin\phi$, as derived in Nakamura and Zhu (2010a). The zonal-mean PV gradient is not a conserved quantity because of the contribution from the curvature of the wave activity profile; it can be modified dramatically in the presence of waves. The Lagrangian-mean PV is conserved for adiabatic, frictionless flow, so its gradient tends to evolve more slowly and systematically, responding only to irreversible mixing and other nonconservative processes.

Figure 6 shows snapshots of the meridional gradients of the two mean PV fields for the initial and final day of each experiment. On day 1 (left) the fields all appear indistinguishable since the initial conditions for each experiment are very similar and essentially zonally symmetric. We see a localized maximum of the PV gradient near 45°N at approximately 8 km, close to the axis of jet. This distribution will tend to focus waves into the jet, making the jet a strong waveguide for the growing eddies. The final distribution of PV in each case shows reduction in the meridional extent of the region of strong gradients, associated with sharpening of the jets. The Lagrangian-mean PV increases monotonically with equivalent latitude by construction and indicates sharper gradients than the zonal mean. The Eulerian, zonal-mean PV gradients are reversed on the flanks of the jet by the end of the simulation and have somewhat smaller maximum value.

The set of panels farthest right in Fig. 6 shows the difference between the initial and final distributions of PV gradients (day 30 − day 1). Here we see that the two life cycles result in oppositely signed dipole anomalies in the upper troposphere, with a node near the initial jet

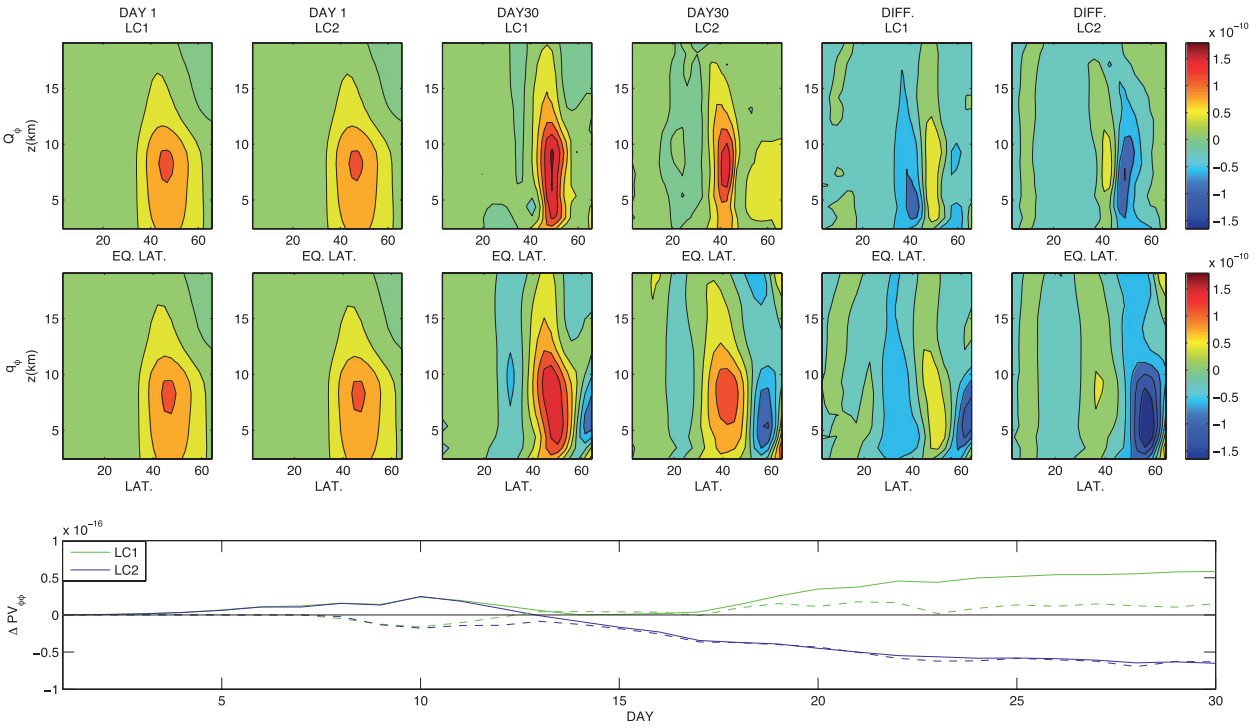

FIG. 6. Contours of the meridional gradients of PV, both the (bottom) zonal and (top) Lagrangian mean, are displayed for (left pair) day 1 and (middle pair) day 30, and (right pair) their difference (day 30 − day 1). For both snapshots of the LC1 and LC2 experiments, the PV gradients are all plotted with the same color bar in units of $m^{-1}\ s^{-1}$. Below are time series of the $\Delta PV_{\phi\phi}$, the change in curvature of PV at the initial jet axis, Lagrangian mean (solid) and zonal mean (dashed), for the entire 30 days of each experiment.

axis. These patterns reflect the fact that the region of enhanced PV gradient is closely associated with the jet, which shifts oppositely in latitude over the course of the two life cycles. The two averages portray fairly consistent changes, although the dipole patterns are narrower in equivalent latitude because of the sharper final $Q_{\phi_{eq}}$ distributions. The largest discrepancies are seen at high latitudes in the LC2 experiment, where waves continue to contribute to the zonal-mean PV gradients on day 30. This dipole pattern in PV gradient depicts a change in the curvature of the mean PV near the initial axis of the jet. An alternate metric for the shift of the jet can then be calculated both from the Lagrangian and zonal means:

$$\Delta PV_{\phi\phi}(t) = \frac{1}{a^2}\int_5^{10} \frac{\partial^2}{\partial\phi^2}[PV(z,t) - PV(z,0)]|_{45N}\, dz. \tag{20}$$

The panel at the bottom of Fig. 6 shows $\Delta PV_{\phi\phi}$, the change in the mean tropospheric curvature of PV at the initial jet axis as a function of time, for both experiments. The Lagrangian-mean PV (solid curves) indicates enhanced curvature in both cases until day 13 when the two life cycles diverge from one another. After day 13 the PV gradient on the poleward flank of the jet begins to decrease in LC2, ultimately resulting in the observed dipole and decreased curvature relative to the initial state. In contrast, the LC1 change in PV curvature remains positive, rising to its peak value after day 22. The corresponding diagnosis using $\overline{q}$ is plotted in dashed curves, indicating similar conclusions about the temporal development but smaller signal in the LC1 case. In the discussion section we will employ $\Delta PV_{\phi\phi}$ to characterize the jet shift resulting from the two life cycles and utilize the association between maximum $Q(\phi_{eq})$ gradients and the jet axis to define a wave index.

5. The effects of increasing barotropic shear and varying zonal wavenumber

In Fig. 7 the time evolution of the global mean wave activity is plotted for three selected wavenumbers at a range of barotropic shears. Within this range of values for U_s (0–12 m s^{-1}) we see a clear progression in the behavior at these wavenumbers ($m = 5, 6, 7$). These plots are similar to those of Hartmann and Zuercher (1998), who plotted eddy kinetic energy for a wavenumber-6 disturbance growing in a similar background flow and calculated the relevant energy conversion terms in order to diagnose the evolution of the flow. The initial stage of

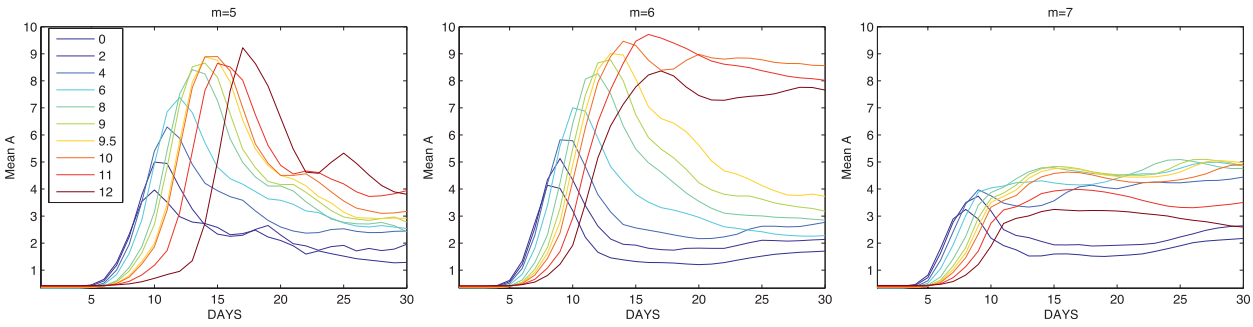

FIG. 7. Each panel depicts the time evolution of the global mean wave activity for a single zonal wavenumber: (left) $m = 5$, (middle) $m = 6$, and (right) $m = 7$. The 10 curves represent different values of the barotropic shear parameter U_s between 0 and 12 m s^{-1} (darker red colors indicate higher shear).

exponential growth is due to baroclinic conversion through eddy heat flux and is very similar for both life cycles. The subsequent barotropic decay phase characterized by large eddy momentum fluxes is very different in the two life cycles. LC2 exhibits much less barotropic conversion during this second phase of the life cycle (Hartmann and Zuercher).

On the left, time series for wavenumber 5 clearly depict the conventional LC1 progression. The initial period of exponential growth is clear, followed by a wave breaking instability, which results in a dissipation of wave activity until a new quasi-steady state is achieved. This dissipation of wave activity is associated with an exchange of pseudomomentum for angular momentum, resulting in the observed changes in the zonal mean wind (Fig. 1). The growth of the instability is delayed with increasing shear (redder colored curves indicate higher U_s). Also the maximum global mean wave activity attained generally increases with greater shear. The tendency of decreasing growth rate with rising shear, observed at $m = 5$, persists for all higher wavenumbers examined in this study. The maximum global mean wave activity attained is a complicated story, which will not be addressed in this study.

The cases examined in detail were wavenumber-6 perturbations, which are plotted in the middle. Here we see the transition from LC1 to LC2 as the $U_s = 9.5$ m s^{-1} (yellow) diverges from $U_s = 10$ m s^{-1} (orange) after day 13. The LC2 cases, initialized with $U_s \geq 10$ m s^{-1}, exhibit less dissipation of wave activity after the peak of the life cycle than the experiments with slightly lower barotropic shear. Even the very low shear cases (darker blue colors), which attain only half of the peak amplitude of the LC2 cases, exhibit greater dissipation in the immediate aftermath of their exponential growth phase. Finally, the $m = 7$ case is plotted in the right panel. The two experiments with lowest initial barotropic shear still exhibit LC1. However, all $m = 7$ cases with $U_s \geq 4$ m s^{-1} develop as LC2. These $m = 7$ cases attain lower maximum amplitudes than the corresponding longer wavelength perturbations and peak earlier, with their exponential growth phase ending prior to day 10 for almost all cases. The LC2 experiments can actually exhibit increasing pseudomomentum after the period of normal mode growth, as seen in these $m = 7$ time series, although that growth is not systematic nor a large fraction of the total wave activity. All simulations for higher wavenumbers exhibited the LC2, with smaller peak values of A and little or no dissipation.

To objectively distinguish the two life cycles, for every one of these simulated cases, we cannot simply rely on the magnitude of wave activity alone. The maximum amplitude of the waves decreases dramatically with increasing wavenumber, so the temporal and spatial domain-averaged wave activity convolves the issues of persistence and peak amplitude. The fundamental distinction between the LC1 and LC2 cases is the extent of wave breaking on the equatorward flank of the jet, as illustrated by Thorncroft et al. (1993). In LC1 filaments of PV are sheared out to the south of the jet where they dissipate over time. The LC2 case is distinguished by a general absence of this equatorward wave propagation and subsequent breaking. So, we can define an index that quantifies the fraction of wave activity found on the equatorward side of the jet axis:

$$\mathrm{WI}(t) = \frac{\int_0^{z_T}\int_0^{J(z,t)} A(\phi_{\mathrm{eq}}, z, t)\, d\phi_{\mathrm{eq}}\, dz}{\iint A\, d\phi_{\mathrm{eq}}\, dz}, \qquad (21)$$

where the axis of the jet is defined as $J(z,t) = \max_{\phi_{\mathrm{eq}}}\{\partial Q/\partial\phi_{\mathrm{eq}}\}$, the equivalent latitude of maximum PV gradient. This index is similar to a quantity considered by Magnusdottir and Haynes (1996), but they employed a fixed latitude to distinguish the two flanks of the jet.

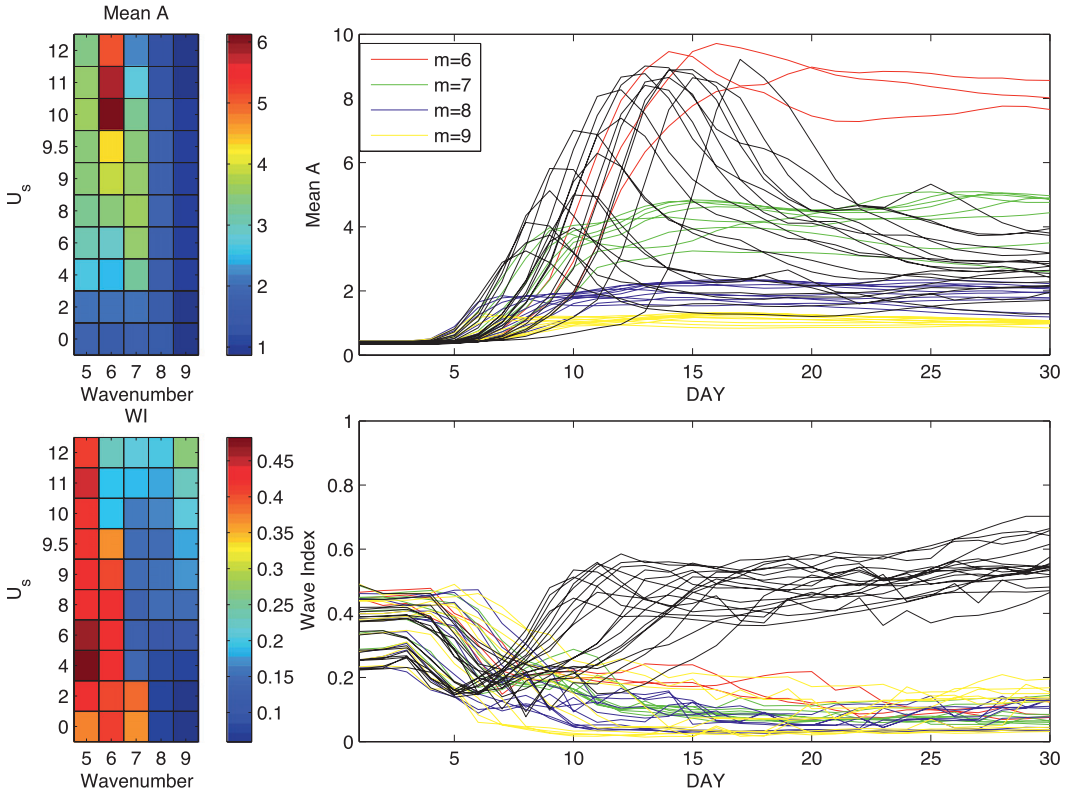

FIG. 8. (top) Time-mean, global-mean wave activity (m s^{-1}) for (left) each case, and (right) the time evolution for all cases. The colored curves are associated with LC2 and the black curves are LC1. (bottom) As for top, but for WI.

In Fig. 8 both wave index (WI) and the domain-averaged wave activity are plotted for each case examined. In the left column we see the time average of each diagnostic, plotted with a distinct color for each case. The mean wave activity (top left) does not vary consistently for all cases, although a general tendency toward lower values with increasing wavenumber is apparent. A related parameter space, spanned by eddy kinetic energy and frequency, was explored in Riviere and Orlanski (2007), who found that long waves break only anticyclonically, while shorter wavelengths may follow either life cycle. Clearly WI (bottom left) distinguishes the two life cycles, with LC1 in red hues and LC2 in darker blue shades. An oblique separatrix between the two life cycles can now be discerned. This parameter space is partitioned into an LC1 region spanned by low zonal wavenumbers and low values of barotropic shear and an LC2 region representing the high shear or high wavenumber cases. Transitions from LC1 to LC2 with increasing shear are seen for both $m = 6$ and $m = 7$, with higher wavenumbers exhibiting only LC2. It is possible that $m = 5$ would exhibit a transition to LC2 if even higher values of initial barotropic shear were applied, but no such behavior was observed for the shear range examined.

The panels on the right show time series of these two metrics for each experiment. Here the LC2 cases have been highlighted in colors by wavenumber and the LC1 cases are plotted in black. In the top panel the global mean wave activity illustrates that the LC2 cases cluster tightly according to wavenumber and clearly lack the strong dissipation seen in the LC1 cases. However, the range of mean wave activities for the LC2 cases cannot be distinguished from that of the LC1 cases. Index WI (bottom) more clearly distinguishes the two cases, with essentially distinct ranges of values after day 10. The wavenumber-5 cases do not break until somewhat later, rising to values of WI ≥ 0.3 between days 10 and 15, but aside from those few cases the black curves are clearly separated from the colored curves by day 10. For all LC2 cases WI diminishes, nearly monotonically, throughout the course of the experiment, asymptotically approaching values below 0.2. Hence the tendency of WI during the eddy growth phase (days 6–10 or so, depending on wavenumber and background shear) has opposite signs for the two life cycles. This fact can be used to predict the subsequent evolution of the instability and the consequent changes in mean wind. Similar indices of wave propagation and breaking have been constructed in Esler and Haynes (1999) and Strong and Magnusdottir

(2008), which proved to be useful predictors for the phase of the observed annular mode.

6. Discussion

The ultimate goal of this investigation was to provide a method for predicting the type of life cycle resulting from a given initial condition. This goal was not attained and questions still remain about the critical factor leading to symmetry breaking in the evolution of this instability. However, as observed by many previous authors (e.g., Thorncroft et al. 1993; Hartmann and Zuercher 1998), the life cycles clearly distinguish themselves during the growth and propagation phase prior to attaining their maximum amplitude and breaking. The fact that this occurs before any significant redistribution of angular momentum or shift of the jet implies that there is some predictive potential to be derived from the distribution of wave activity. The figure below illustrates the shift of the jet after the onset of wave breaking, measured by $\Delta PV_{\phi\phi}$, as a function of the tendency of WI a week or more earlier in the life cycle. Here the tendency of WI is simply calculated as a finite difference, two days before the maximum in wave activity is reached. Because of the difference in growth rates between the long waves (m = 5, 6) and the shorter waves (m = 7, 8, 9), these characteristic metrics for the life cycles had to be calculated during different intervals. For the short waves, which grow more rapidly, the tendency of WI was calculated on or prior to day 6, and the PV curvature on day 14. For the long waves WI_t was calculated before day 12, and $\Delta PV_{\phi\phi}$ on day 18. Although the timing of the life cycles differs with wavenumber, they all suggest about a week lag between the propagation of waves relative to the jet axis and the ultimate shift of the jet.

In Fig. 9, several clusters of points can be distinguished, with the filled circles calculated using the Lagrangian diagnostics and open circles based on an Eulerian metric for comparison. The filled green circles, reflecting LC1 experiments, all plot in the first quadrant. This implies that the equatorward propagation of wave activity early in the life cycle invariably precedes a poleward shift of the jet by about a week. The filled blue circles, LC2 experiments, generally plot in the third quadrant. This suggests that the negative tendency of WI is a strong indicator of a coming equatorward shift of the jet. The two marginal cases (points in the second and fourth quadrants) are m = 7, which falls somewhere between long and short baroclinic waves, so the timing of their life cycles did not conform to these conventions, although their overall behavior still supports the broader conclusions. Plotted in black are the pair of m = 6 transition cases examined in detail. The two cases depict

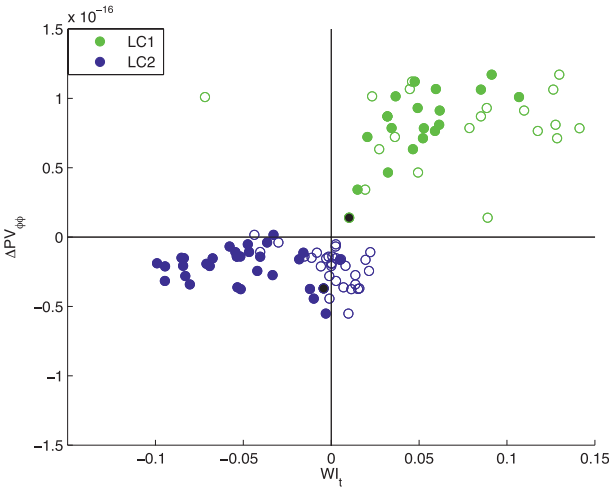

FIG. 9. The change in PV curvature at the initial jet axis: $\Delta PV_{\phi\phi}$ (m^{-2} s^{-1}) is plotted as a function of the tendency of the wave index during the eddy growth phase WI_t (day^{-1}) for each of the 50 experiments. Filled circles are calculated from the Lagrangian-mean diagnostic WI_t; open circles reflect a corresponding Eulerian metric based on EKE. Green symbols are LC1 experiments, blue are LC2, and the pair of cases examined in detail is plotted in black.

small magnitude and differing signs of WI tendency on day 11 and opposite shifts of the jet by day 18. That the wave propagation is so weak in this pair of transition cases when compared with the tendency of WI for cases that are not as close to the abrupt transition between life cycles suggests that a threshold in wave propagation distinguishes the two life cycles.

The predictive diagnostic WI_t required several pieces of Lagrangian data. The distribution of wave activity in the equivalent latitude meridional plane is a Lagrangian-mean diagnostic, which is more robust than its Eulerian counterparts (eddy kinetic energy, linear zonal mean pseudomomentum) (Solomon and Nakamura 2012). The jet latitude $J(z, t)$ has been defined in terms of the maximum gradient of Lagrangian-mean PV, primarily for the practical purpose of determining the location of the jet in terms of equivalent latitude. Also, the eddy propagation phase was determined based on the timing of maximum of wave activity for each life cycle. To determine how important this Lagrangian information is we considered an Eulerian diagnostic (open circles), plotted for comparison with WI_t. This metric employs eddy kinetic energy in place of wave activity—the jet latitude defined as the maximum of the zonal mean wind and timing based on the maximum of mean EKE during the life cycle. Linear zonal-mean pseudomomentum is unsuitable for this type of analysis because of the vanishing $\overline{q}$ gradient, which makes it impossible to calculate domain averages since the linear pseudomomentum becomes infinite. From Fig. 9 we can see that the Eulerian

diagnostic is not able to distinguish the two life cycles, with the majority of LC2 cases exhibiting increasing EKE south of the latitude of maximum winds (open circles in the second quadrant). The timing of maximum EKE is fairly consistent with wave activity, although A tends to develop more smoothly and shows less dissipation in the LC2 cases (not shown). The distribution of eddies relative to the maximum PV gradient seems to be a more reliable discriminant between the two life cycles than the distribution with respect to the maximum winds. This supports the perspective that the mixing of PV by eddies and resultant modification of the PV gradient is as fundamental to the dichotomy between life cycles as the flux of momentum.

7. Conclusions

The use of Lagrangian-mean wave activity provides insights into the evolution of baroclinic eddies in these life cycle experiments. The use of a conservative diagnostic allows easier quantification of the spatiotemporal evolution of wave activity density than conventional Eulerian diagnostics. Measures such as eddy kinetic energy only provide robust information in the domain average. Lagrangian-mean finite-amplitude wave activity can illustrate the specific regions of the domain whose circulation is being modified by the presence of waves as well as reproduce prior conclusions about the temporal evolution of domain-average pseudomomentum. Domain average A clearly depicts the initial period of exponential growth common to both life cycles and the subsequent dichotomy in trajectories, with dissipation in LC1 and persistence in LC2. The spatial distribution explains this difference, underscoring the equatorward breaking of waves in LC1 and the consequent deceleration on the south flank of the jet, resulting in the apparent poleward shift of the jet. In contrast, LC2 evolution involves little or no equatorward wave breaking, hence no significant redistribution of angular momentum toward higher latitudes.

The index of refraction has been used in previous studies to illustrate the role of critical lines and wave reflection in the evolution of life cycle experiments (Thorncroft et al. 1993; Hartmann and Zuercher 1998; Limpasuvan and Hartmann 2000). Such indices rely heavily on the gradient of zonal-mean potential vorticity, which provides the restoring force that permits Rossby wave propagation. In the presence of finite amplitude waves the gradients of PV can become obscured by zonal averaging, making it difficult to interpret the index of refraction and impossible to compute the linear pseudomomentum. In this study we considered the meridional gradient of Lagrangian-mean potential vorticity, which can only be modified through irreversible processes such as mixing. The Lagrangian-mean PV depicts the progressive evolution of a localized maximum in the PV gradient, which is associated with the curvature of the evolving jet. LC1 results in significant mixing on the equatorward flank of the jet, increasing the meridional PV gradient and sharpening the jet, whose mean latitude shifts toward the pole. In contrast, LC2 produces more mixing on the poleward flank of the jet, which also enhances the maximum PV gradient, concentrating it to the south of the original jet axis and diminishing the mean gradient to the north. This provides a context for thinking about baroclinic eddy life cycles in terms of mixing and PV staircases (Dritschel and McIntyre 2008; Nakamura and Zhu 2010b).

Perhaps the most useful outcome of this study is a simple wave index, which utilizes both Lagrangian-mean wave activity and a Lagrangian perspective of jet location, thereby providing a clear distinction between the two life cycles. We have demonstrated that, in a broad suite of simulations, the tendency of this index can be used to predict the subsequent evolution of the instability and, hence, the shift of the jet. The use of a Lagrangian perspective of jet axis location, via the maximum PV gradient in equivalent latitude, turns out to be a crucial piece of this construction and makes this diagnostic more applicable to the range of dynamics that might be encountered in observations than a fixed Eulerian prescription of jet latitude (e.g., Magnusdottir and Haynes 1996). A future study will apply this wave index to observational reanalysis in order to advance our understanding of the role which wave breaking plays in annular mode variability.

Acknowledgments. Thanks to the anonymous reviewers whose feedback contributed to the revision of this paper. The lead author is supported by NSF Grant ATM-0947837. Dr. Gang Chen is supported by NSF Grant AGS-1064079. Dr. Jian Lu is supported by NSF Grant AGS-1064045.

REFERENCES

Benedict, J. J., S. Lee, and S. B. Feldstein, 2004: Synoptic view of the North Atlantic Oscillation. *J. Atmos. Sci.,* **61,** 121–144.

Butchart, N., and E. E. Remsberg, 1986: The area of the stratospheric polar vortex as a diagnostic for tracer transport on an isentropic surface. *J. Atmos. Sci.,* **43,** 1319–1339.

Dritschel, D. G., and M. E. McIntyre, 2008: Multiple jets as PV staircases: The Phillips effect and the resilience of eddy-transport barriers. *J. Atmos. Sci.,* **65,** 855–874.

Esler, J. G., and P. H. Haynes, 1999: Baroclinic wave breaking and the internal variability of the tropospheric circulation. *J. Atmos. Sci.,* **56,** 4014–4031.

Hartmann, D. L., and P. Zuercher, 1998: Response of baroclinic life cycles to barotropic shear. *J. Atmos. Sci.,* **55,** 297–313.

Karoly, D. J., and B. J. Hoskins, 1982: Three-dimensional propagation of planetary waves. *J. Meteor. Soc. Japan,* **60,** 109–123.

Killworth, P. D., and M. E. McIntyre, 1985: Do Rossby-wave critical layers absorb, reflect or over-reflect? *J. Fluid Mech.,* **161,** 449–492.

Limpasuvan, V., and D. L. Hartmann, 2000: Wave-maintained annular modes of climate variability. *J. Climate,* **13,** 4414–4429.

Lorenz, D. J., and D. L. Hartmann, 2001: Eddy–zonal flow feedback in the Southern Hemisphere. *J. Atmos. Sci.,* **58,** 3312–3327.

Magnusdottir, G., and P. H. Haynes, 1996: Wave activity diagnostics applied to baroclinic wave life cycles. *J. Atmos. Sci.,* **53,** 2317–2353.

McIntyre, M. E., and T. N. Palmer, 1983: Breaking planetary waves in the stratosphere. *Nature,* **305,** 593–600.

Nakamura, N., and A. Solomon, 2010: Finite-amplitude wave activity and mean flow adjustments in the atmospheric general circulation. Part I: Quasigeostophic theory and analysis. *J. Atmos. Sci.,* **67,** 3967–3983.

——, and D. Zhu, 2010a: Finite-amplitude wave activity and diffusive flux of potential vorticity in eddy–mean flow interactions. *J. Atmos. Sci.,* **67,** 2701–2716.

——, and ——, 2010b: Formation of jets through mixing and forcing of potential vorticity: Analysis and parameterization of beta-plane turbulence. *J. Atmos. Sci.,* **67,** 2717–2733.

Pfeffer, R. L., 1987: Comparison of conventional and transformed Eulerian diagnostics in the troposphere. *Quart. J. Roy. Meteor. Soc.,* **113,** 237–254.

Polvani, L. M., and J. G. Esler, 2007: Transport and mixing of chemical air masses in idealized baroclinic life cycles. *J. Geophys. Res.,* **112,** D23102, doi:10.1029/2007JD008555.

Riviere, G., and I. Orlanski, 2007: Characteristics of the Atlantic storm-track eddy activity and its relation with the North Atlantic oscillation. *J. Atmos. Sci.,* **64,** 241–266.

Simmons, A. J., and B. J. Hoskins, 1980: Barotropic influences on the growth and decay of nonlinear baroclinic waves. *J. Atmos. Sci.,* **37,** 1679–1684.

Solomon, A., and N. Nakamura, 2012: An exact Lagrangian-mean wave activity for finite-amplitude disturbances to barotropic flow on a sphere. *J. Fluid Mech.,* **693,** 69–92.

Strong, C., and G. Magnusdottir, 2008: Tropospheric Rossby wave breaking and the NAO/NAM. *J. Atmos. Sci.,* **65,** 2861–2876.

Thorncroft, C. D., B. J. Hoskins, and M. E. McIntyre, 1993: Two paradigms of baroclinic-wave life-cycle behaviour. *Quart. J. Roy. Meteor. Soc.,* **119,** 17–55.

Vallis, G. K., E. P. Gerber, P. J. Kushner, and B. A. Cash, 2004: A mechanism and simple model of the North Atlantic oscillation and annular modes. *J. Atmos. Sci.,* **61,** 264–280.